A signal processing framework for simultaneous detection of multiple environmental contaminants

2013 Meas. Sci. Technol. 24 115102

(http://iopscience.iop.org/0957-0233/24/11/115102)

Meas. Sci. Technol. **24** (2013) 115102 (11pp) doi:10.1088/0957-0233/24/11/115102

A signal processing framework for simultaneous detection of multiple environmental contaminants

Subhadeep Chakraborty[1], **Michael P Manahan**[2] **and Matthew M Mench**[1,3]

[1] Department of Mechanical, Aerospace and Biomedical Engineering, University of Tennessee, Knoxville, TN, USA
[2] Department of Mechanical and Nuclear Engineering, The Pennsylvania State University, University Park, PA, USA
[3] Emissions and Catalysis Research Group, ORNL, Oak Ridge, TN 37831, USA

E-mail: schakrab@utk.edu, manahan@psu.edu and mmench@utk.edu

Received 21 May 2013, in final form 2 September 2013
Published 1 October 2013
Online at stacks.iop.org/MST/24/115102

Abstract
The possibility of large-scale attacks using chemical warfare agents (CWAs) has exposed the critical need for fundamental research enabling the reliable, unambiguous and early detection of trace CWAs and toxic industrial chemicals. This paper presents a unique approach for the identification and classification of simultaneously present multiple environmental contaminants by perturbing an electrochemical (EC) sensor with an oscillating potential for the extraction of statistically rich information from the current response. The dynamic response, being a function of the degree and mechanism of contamination, is then processed with a symbolic dynamic filter for the extraction of representative patterns, which are then classified using a trained neural network. The approach presented in this paper promises to extend the sensing power and sensitivity of these EC sensors by augmenting and complementing sensor technology with state-of-the-art embedded real-time signal processing capabilities.

Keywords: electrochemical sensor, environmental contaminants, symbolic dynamics

(Some figures may appear in colour only in the online journal)

1. Introduction

The US defense establishments have long considered the possible use of chemical warfare agents (CWAs) and thus have continued efforts to develop sensors for the ambient detection of CWAs to protect troops in battlefields as well as sensors suitable for civilian use in places such as airports, railroad stations, large public and private office buildings, theaters, sports arenas, etc.

Intense research efforts in the past have led to the development of several sophisticated analytical and measurement techniques, broad and vast in types, applications and methods. Several thorough review papers detail thousands of papers in the field in the past two decades [1–3]. A subset of chemical sensors are electrochemical (EC) sensors, which have two principal modes of electroanalytic measurement: potentiometric and amperometric [4]. Potentiometric analysis uses the equilibrium potential of a given electrode to determine the presence of an ionic specie. The electrode must be carefully chosen such that its interaction with the ion of interest can be predicted and the corresponding ion concentration can be determined. Typically, this class of sensors has detection limits of the order of 100 nanomoles per liter of the concentration of the ion present in a particular oxidation state [5]. Alternatively, amperometric measurement techniques monitor the current as a function of the applied potential. By varying the applied potential, multiple species can be detected by one sensor, and typically the detection limits are lower than that of potentiometric techniques [5].

For environmental monitoring applications, simultaneous, multi-species gas detection is desirable. However, due to the variability of contaminant concentration, coupled with

the presence of multiple confounding contaminant species and the variation of other key variables such as flow rate, temperature and relative humidity (RH) [6–10], accurate detection and determination can become quickly convoluted and imprecise. Some groups have used potentiometric measurement techniques for the detection of single gases [11–13], whereas most groups use amperometric measurement techniques coupled with signal processing to delineate the specific cases for gas detection [8–10, 14–16].

This paper describes an onboard real-time signal processing technique to extract statistically significant low-dimensional characteristic patterns from dynamic responses of sensors exposed to contaminant vapors. Three gases, N_2, H_2, CO, and mixtures of these gases in varying proportions were used as contaminants to demonstrate proof-of-concept. Even though chemically very distinct from the CWAs, these gases serve to demonstrate the efficacy of the algorithm in identifying and correctly classifying mixtures of gases, a capability crucial for real world application of sensors.

The results obtained promise to extend the sensing power and sensitiveness of EC sensors by augmenting and complementing the sensor technology with state-of-the-art embedded real-time signal processing capabilities. In order to identify a broad range of contaminants, it is clear that both physical insight into the underlying EC processes and advanced signal processing techniques need to be further developed and employed simultaneously.

2. Technical approach

An EC sensor consists of electrodes (e.g., working electrode, counter electrode and reference electrode). Gaseous species diffuse to the electrodes where the species are either oxidized or reduced. The potential difference between the working electrode and the counter electrode (in a two-electrode system, for example) can be quantified by the Nernst equation and depends on the species present at each electrode. If an external circuit controls the potential across the sensor, then the resulting electrical current that is passed through the external circuit can be measured. The current response, being highly sensitive to the potential difference across the sensor and therefore to the species present, forms the basis of amperometric species detection techniques, which performs efficiently as long as the target gases have substantially different amperometric signatures.

At the root of this signal processing technique is the idea of perturbing an EC sensor with an oscillating potential rather than static voltage levels for the extraction of statistically rich information from the current response. The dynamic response is a function of the degree and mechanism of contamination by different species, and therefore carries signatures of the operating condition which can be extracted in the form of low-dimensional pattern vectors for the correct classification of gases.

For the purpose of extracting relevant patterns from the current response, a variety of pattern extraction and classification tools are available, each with certain strengths and weaknesses. Pattern recognition methods such as Bayesian filtering, which is both model-based and dynamic data-driven, is capable of detecting parametric or nonparametric changes in the model; however, a sufficiently accurate model needs to be available. The Kalman (extended Kalman) filter [17] is often adequate for linear (linearized) systems, but it may fail to capture the dynamics of a nonlinear system, specifically with non-additive uncertainties [18]. Recent literature has reported Monte Carlo Markov chain techniques such as particle filtering (PF) [19], and sigma point techniques such as unscented Kalman filtering (UKF) [20] that yield numerical solutions to Bayesian state estimation problems and have been applied for pattern detection in nonlinear dynamical systems [21]. Both UKF and PF are elegant methods which perform well in a variety of problems but may suffer from high memory requirements and long execution times.

In addition to Bayesian filtering, there exist other classes of well-known pattern recognition tools such as artificial neural networks (ANN), principal component analysis (PCA) and Kernel regression analysis (KRA) for pattern change detection [22]. In the class of ANN, mutilayer perceptron [23] and radial basis function [24] configurations have been widely used for the detection of anomalous patterns. PCA [25] and KRA [26] are also commonly used for data-driven pattern recognition.

In this paper, a recently reported data driven signal processing algorithm called symbolic dynamic filtering (SDF) has been used for pattern extraction from the current response signals. Rao *et al* [27] have extensively studied the relative advantages and drawbacks of SDF as a pattern extraction tool in comparison to particle filter and unscented Kalman filter as well as ANN and PCA.

The problem of identification of characteristic statistical patterns using SDF is formulated in the following section in terms of observation-based estimation of process variables.

2.1. Pattern extraction with symbolic dynamic filtering

This section presents a brief summary of the underlying concepts and essential features of a novel data-driven pattern identification tool called SDF [28]. The concept of SDF is built upon the principles of several disciplines including symbolic dynamics [29], statistical pattern recognition [30], information theory [31] and probabilistic finite state machines [32].

While the details are reported in recent publications [28], the essential concepts of space partitioning [33], symbol sequence generation, construction of a finite-state machine and pattern recognition, all of which form the backbone of this pattern identification framework, are consolidated here and succinctly described for self-sufficiency and clarity.

2.1.1. Symbolic dynamic encoding. Let $\Omega \in \mathbb{R}^n$ be a compact (i.e., closed and bounded) region, within which the trajectory of the dynamical system is circumscribed. The region Ω is partitioned into a finite number of (mutually exclusive and exhaustive) cells, so as to obtain a coordinate grid. Let the cell, visited by the trajectory at a time instant, be denoted as a random variable taking a symbol value from the alphabet Σ. An orbit of the dynamical system is described by the time series data as $\{x_0, x_1, \ldots, x_k, \ldots\}$ with $x_i \in \Omega$, which passes

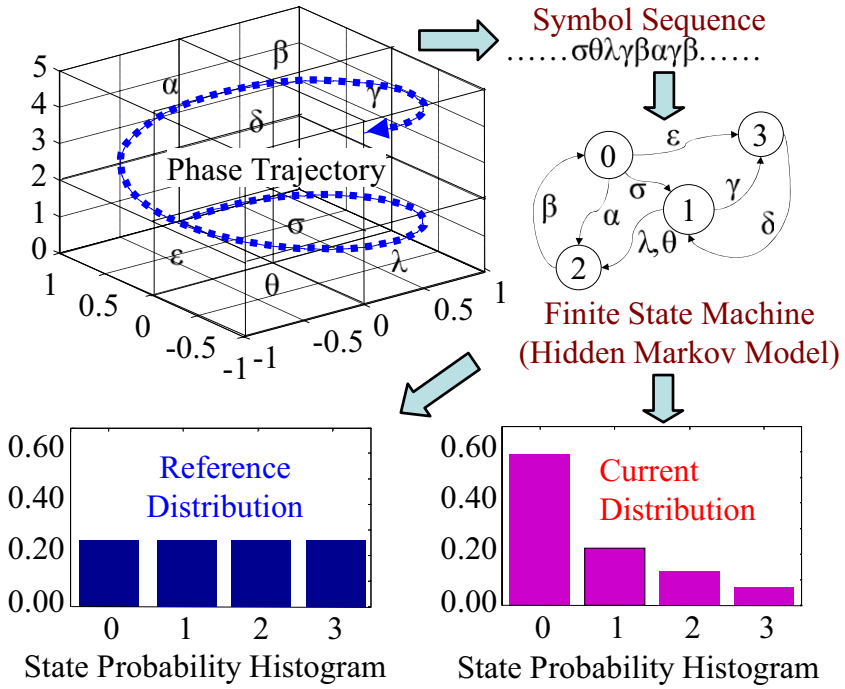

Figure 1. Symbolic time series analysis based pattern identification [34].

through or touches one of the cells of the partition. Each initial state $x_0 \in \Omega$ generates a sequence of symbols defined by a mapping from the phase space into the symbol space as

$$x_0 \to s_0 s_1 s_2 \ldots s_k \ldots, \tag{1}$$

where each s_i, $i = 0, 1, \ldots,$ takes a symbol from the alphabet Σ. The mapping in equation (1) is called *symbolic dynamics* as it attributes a legal (i.e., physically admissible) sequence of symbols to the system dynamics starting from an initial state.

Figure 1 pictorially elucidates the concepts of partitioning a finite region of the phase space and the mapping from the partitioned space into the symbol alphabet. This represents a spatial and temporal discretization of the system dynamics defined by the trajectories. Figure 1 also shows the conversion of the symbol sequence into a finite-state machine and generation of the state probability vectors as explained in the following subsections.

The time series data-set of selected observable outputs such as the current density or the terminal voltages can be used for partitioning and symbolic dynamic encoding (see section 2.2 for further details).

2.2. Analytic signal space partitioning

A crucial step in symbolic time series analysis is the partitioning of the phase space for symbol sequence generation [35]. This paper presents a partitioning method, called analytic signal space partitioning (ASSP) [36, 37], for symbolic time series analysis. The underlying concept of ASSP partitioning is built upon the Hilbert transform of the observed real-valued data sequence into the corresponding complex-valued analytic signal.

The Hilbert transform [38] of a real-valued signal $x(t)$ is defined as

$$\widetilde{x}(t) = \mathcal{H}[x](t) = \frac{1}{\pi} \int_{\mathbb{R}} \frac{x(\tau)}{t - \tau} \mathrm{d}\tau. \tag{2}$$

That is, $\widetilde{x}(t)$ is the convolution of $x(t)$ with $\frac{1}{\pi t}$ over the real field $\mathbb{R}$, which is represented in the Fourier domain as

$$\mathcal{F}[\widetilde{x}](\xi) = -\mathrm{i}\ \mathrm{sgn}(\xi)\ \mathcal{F}[x](\xi), \tag{3}$$

where $\mathrm{sgn}(\xi) = \begin{cases} +1 & \text{if } \xi > 0 \\ -1 & \text{if } \xi < 0 \end{cases}$. The corresponding complex-valued analytic signal is defined as

$$\mathcal{A}[x](t) = x(t) + \mathrm{i}\,\widetilde{x}(t) \qquad \text{and} \tag{4}$$

$$\mathcal{A}[x](t) = A(t)\ \exp(\mathrm{i}\,\varphi(t)), \tag{5}$$

where $A(t)$ and $\varphi(t)$ are called the instantaneous amplitude and instantaneous phase of $\mathcal{A}[x](t)$, respectively.

Given a set of real-valued time series data, the Hilbert transform of this data-set yields a pseudo-phase plot that is constructed from the analytic signal by a bijective mapping of the complex domain onto the $\mathbb{R}^2$, i.e., by plotting the real and imaginary parts of the analytic signal on the x and y axes, respectively. The time-dependent analytic signal in equation (4) is now represented as a (one-dimensional) trajectory in the two-dimensional pseudo-phase space.

Let Ξ be a compact region in the pseudo-phase space, which encloses the trajectory. The objective here is to partition Ξ into finitely many mutually exclusive and exhaustive segments, where each segment is labeled with a symbol. The segments are determined by magnitude and phase of the analytic signal and also from the density of data points in these segments. That is, if the magnitude and phase of a data point of the analytic signal lies within a segment or on its boundary, then that data point is labeled with the corresponding symbol.

This symbol generation process is called ASSP [36] and the resulting set of (finite) symbols is called the alphabet Σ.

One possible way of partitioning Ξ is to divide the magnitude and phase of the time-dependent analytic signal in equation (4) into uniformly spaced segments between their minimum and maximum values. This is called uniform partitioning. An alternative method, known as maximum entropy partitioning [39], maximizes the entropy of the partition, which imposes a uniform probability distribution on the symbols. In this partitioning, parts of the state space with rich information are partitioned into finer segments than those with sparse information. The ASSP algorithm makes use of either one or both of these partitioning methods.

2.3. Probabilistic finite-state machine construction

Using the discrete-time, discrete-valued stochastic sequence created by the ASSP (section 2.2), the state machine is constructed on the principle of sliding block codes [29]. A window of length D on the symbol sequence $\mathbb{S} = \ldots, s_{-2}, s_{-1}, s_0, s_1, s_2, \ldots$ is shifted to the right by one symbol, such that it retains the last $(D-1)$ symbols of the previous state and appends it with the new symbol at the end. The states of the machine are represented by blocks $s_i s_{i+1} s_{i+2} \ldots s_{i+D-1}$ in the symbol sequence. Each state belongs to an equivalence class of strings characterized by a specific word of length D at the leading edge. Thus, with cardinality $|\Sigma|$ of the alphabet and depth D of a symbol string of a state, the total maximum number of states in the D-Markov machine is given by $|\Sigma|^D$. The state machine moves from one state to another upon occurrence of a symbol. All symbol sequences that have the same last D symbols represent the same state. The machine constructed in this fashion is called the D-Markov machine [28], because of its Markov properties.

Definition. *$\mathbb{S} = \ldots, s_{-2}, s_{-1}, s_0, s_1, s_2, \ldots$ is called the Dth order Markov process if the probability of the next symbol depends only on the previous (at most) D symbols, i.e.*

$$P(s_i|s_{i-1}s_i - 2 \ldots s_{i-D} \ldots) = P(s_i|s_{i-1}s_i - 2 \ldots s_{i-D}).$$

The finite-state machine constructed above has D-Markov properties because the probability of occurrence of the symbol σ_{i_ℓ} on a particular state depends only on the configuration of that state, i.e., the previous D symbols. The states of the machine are marked with the corresponding symbolic word permutation and the edges joining the states indicate the occurrence of a symbol σ_{i_ℓ}. The occurrence of a symbol at a state may keep the machine in the same state or move it to a new state.

Definition. *The probability of transitions from the state q_j to the state q_k belonging to the set Q of states under a transition $\delta : Q \times \Sigma \to Q$ is defined as [28]*

$$\pi_{jk} = P(\sigma \in \Sigma \mid \delta(q_j, \sigma) \to q_k); \sum_k \pi_{jk} = 1. \qquad (6)$$

Thus, for D-Markov machines, the irreducible stochastic matrix $\mathbf{\Pi} \equiv [\pi_{ij}]$ describes all transition probabilities between states with at most $|\Sigma|^{D+1}$ nonzero entries.

The time series data at the reference condition (pure H_2), set as a benchmark, generate the *state transition matrix* $\mathbf{\Pi}$ that, in turn, is used to obtain the *state probability vector* $\mathbf{p}$ whose elements are the stationary probabilities of the state vector, where $\mathbf{p}$ is the left eigenvector of $\mathbf{\Pi}$ corresponding to the (unique) unit eigenvalue. The state probability vector $\mathbf{q}$ is obtained from time series data at a (possibly) contaminated condition. The partitioning of time series data and the state machine structure should be the same in both cases, but the respective state transition matrices could be different.

Pattern changes take place in the EC sensor due to parametric variations. These variations are a result of poisoning of the membrane, difference in the diffusion properties of the operating gases, etc. The probability distributions obtained by analyzing the current response for different concentration/composition of contaminants serve as low-dimensional feature vectors which are unique to that particular operating condition.

In light of the above description, the major advantages of SDF which make this technique ideal for the current application are as follows.

- *Robustness to measurement noise and spurious signals.* The procedure of SDF is robust to measurement noise and spurious disturbances and it filters out the noise at different steps. First of all, coarse graining of the continuous data (i.e., partitioning into finite blocks) and generation of a symbol sequence eliminate small measurement noise [28]. Secondly, the Hilbert transform also contributes in the signal–noise separation of the raw time series data [36]. Finally, the state probabilities are generated by passing a long symbol sequence over the finite-state machine, which further eliminates small (zero-mean) measurement noise.
- Adaptability to low-resolution sensing due to coarse graining in space partitions [28].
- Applicability to networked communication systems due to the capability of data compression into low-dimensional pattern vectors and error-free transmission over networked systems. Future research is envisioned in the area.

2.4. Pattern classification with artificial neural networks

The SDF algorithm extracts a low-dimensional feature vector for each operating condition. The next task, that is, pattern recognition and classification, can be completed with a multitude of existing algorithms such as maximum entropy classifiers [40], naive Bayes classifiers [41], decision trees [42], support vector machines [43], kernel estimation [44] and K-nearest-neighbor [45] algorithms as well as neural networks. For the current purpose, a neural network was trained, so that a particular class of pattern vectors representing a specific operating condition leads to a specific target class.

2.5. Classification results

In order to validate the concept of the EC sensor based on SDF, a set of experiments were performed on an EC sensor using H_2 contaminated with CO and N_2 respectively

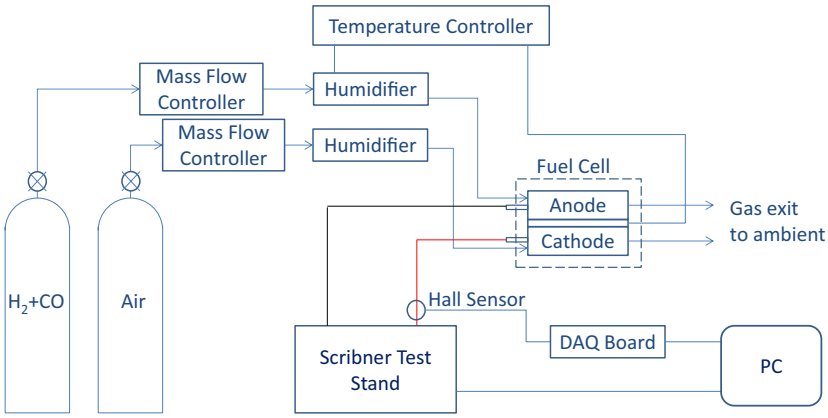

Figure 2. Schematic of the experimental test setup.

at varying contamination levels. Carbon monoxide (CO) and nitrogen (N_2) were chosen to probe the ability of the algorithm to leverage both physical and EC differences between contaminants to make outcome determinations. That is, CO was chosen because it is known to chemisorb onto the surface of the platinum in the polymer electrolyte fuel cell (PEFC) catalyst layer [46], even at very low concentrations, thus poisoning the catalyst layer. Such small concentrations (up to 20 ppm shown here), however, have virtually no effect on the diffusion of hydrogen to the catalyst layer. Therefore, CO represents a family of contaminants that interact in a purely EC manner (chemisorption) with negligible effects on the diffusion of hydrogen. Conversely, N_2 is known to have no adsorption effect on the platinum catalyst layer within the operating conditions of the PEFC. With 25% N_2 content in the anode gas stream, however, the diffusion of hydrogen to the anode catalyst layer is drastically inhibited. Thus, the N_2 represents a family of contaminants that alter the diffusion of the electrochemically active species (in this case, hydrogen) to the catalyst layer, yet do not significantly adsorb on the catalyst layer.

2.5.1. Experimental setup. Experiments were performed using a 850 C fuel cell test station (Scribner Associates Inc.) and a 5 cm^2 fuel cell with serpentine channels (Fuel Cell Technologies Inc.). A commercially available membrane electrode assembly (MEA) with symmetrical Pt loading of 0.3 mg Pt cm^{-2} was used in the cell. The SGL 10 BB-type diffusion media were used with a microporous layer and hydrophobic treatment. Anode and cathode humidifier temperatures were controlled to meet a specific RH value at the operating temperature.

Figure 2 shows the experimental arrangement used in the validation of the sensor. Ultra high purity hydrogen (99.999%) and certified hydrogen gas bottles with premixed CO, supplied by Airgas Inc., were used for the experiments. Flow rates were controlled with calibrated mass flow controllers.

2.5.2. Measurement and data analysis. In all the experiments, the flow rates on the anode and cathode were kept constant at 69 and 250 standard cm^3 min^{-1} (sccm), respectively, which corresponded to a stoichiometry of 2 and 3 at 1 A cm^{-2}. During the experiment, the cell temperature was maintained at 65 °C. Humidification temperatures were maintained such that RH at the anode and cathode inlets were 88% and 100% RH, respectively.

The polarization curves were obtained by running in galvanostatic mode, dwelling at each current step for 1 min in order to reduce the small timescale transients. Voltage values reported at each step were averaged over the duration of the step. Finer steps were used in the low current density region where changes in voltage are more rapid due to kinetic changes. Also, for the contaminated polarization curves, finer steps were used to improve resolution of performance.

In figure 3, selected polarization curves indicate the performance of the fuel cell with pure hydrogen on the anode, hydrogen contaminated with 20 ppm CO and hydrogen contaminated with 25% N_2. The three curves indicate the fundamental difference of the two contaminants: CO chemisorbs onto the catalyst surface, severely reducing the performance of the cell. Nitrogen inhibits hydrogen gas diffusion to the electrode, which affects the mass-transport behavior at higher current; as shown, currents higher than 1.3 A cm^{-2} could not be sustained because of the diffusion limitation.

In order to generate the time series data of current for each CO level, it is necessary to perturb the EC system using a voltage pulse when the sensor reaches a poisoned steady state. For that purpose, an input voltage pulse, alternating between 0.65 and 0.45 V repeatedly with a 5 s dwell time at each value, was used to excite the sensor. The input voltage cycle was the same for the healthy (i.e. pure H_2) system, for different CO levels and for different levels of N_2 contamination.

Current response was measured using a Tektronix AMA6302 Hall effect current probe, at a sampling frequency of 30 Hz. A time series containing a total of 10 000 data points was collected over 50 cycles. The time series data were analyzed using the SDF method to extract the characteristic pattern vector for each contamination level and species.

Figure 4 shows the dynamic current response of the fuel cell when the applied potential was switched between 0.65 and 0.45 V as indicated on the secondary *x*-axis. In all cases, the uncontaminated cell yields the highest current, as expected.

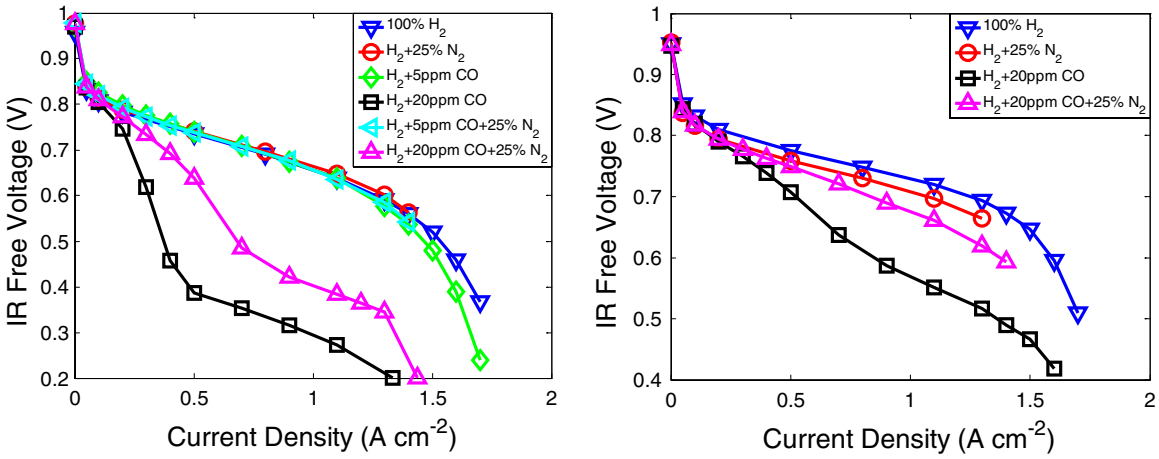

Figure 3. Polarization curves at (*a*) 65 °C and (*b*) 75 °C.

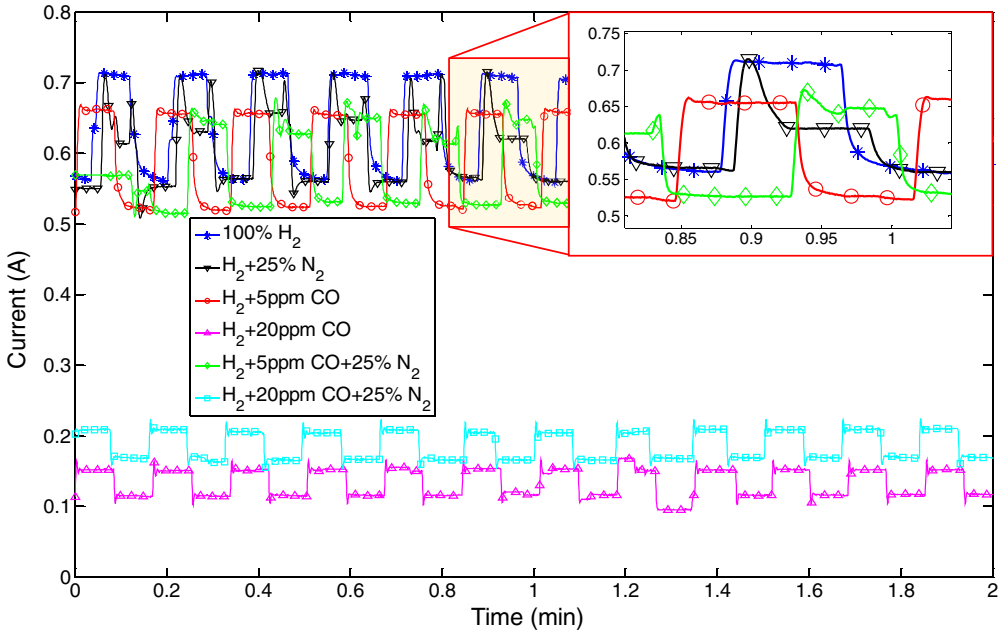

Figure 4. Current response of the EC sensor for the voltage pulse (65 °C) for 0, 5 and 20 ppm CO, 25% N_2 and the mixture of these gases.

When poisoned with CO, the current is stable but altered. There is a drastic reduction in current with 20 ppm CO due to the high surface coverage of CO at the catalyst surface. When the anode gas stream is contaminated with N_2, a unique signal is observed. The current is stable when the applied voltage is 0.65 V, indicating that the diffusion of hydrogen through the nitrogen environment is sufficient to sustain the demand of the applied potential. With higher concentrations of nitrogen, lower current is expectedly observed, indicating the inhibited diffusion and reduced concentration of hydrogen. At 0.45 V with N_2 contamination, the signal fluctuates and decreases with time because the diffusion of H_2 through the N_2 inert gas cannot sustain the EC reaction. That is, the hydrogen at the catalyst surface is completely consumed, and the mass-transport of hydrogen through nitrogen becomes the limitation. This mass-transport-limited condition was also observed in the polarization curves (figure 3), noting that currents higher than 1.3 A cm^{-2} were not obtainable with 25% N_2 in the anode gas stream. In general, the current response to a step change in voltage is a function of various physicochemical phenomena, which generally have different timescales. For example, all diffusive mass-transport processes through liquid, gas and ionomer phases are dependent on the environmental conditions and are relatively slow responses compared to charge transport and EC kinetic processes. Other phenomena such as adsorption/desorption, heat transfer and ion transfer in the electrolyte also occur with different response times. The result is a time varying response that is rich in data that can be used as a diagnostic tool with proper signal processing to distinguish between these various timescale-dependent processes. The key idea is thus the use of different voltage step changes to stimulate unique current responses which can be used to separate these processes and indicate the extent to which they have been altered by the environmental conditions (e.g., gaseous poison).

2.5.3. Signal processing with SDF. The top row of figure 5 exhibits the current response recorded by perturbing the sensor

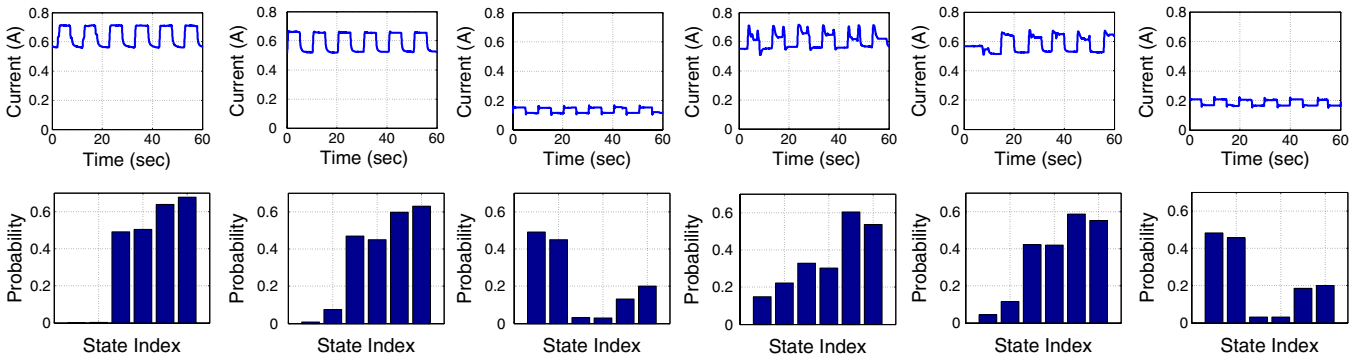

Figure 5. Row (1): current response of the EC sensor for (left to right) pure H_2, $H_2 + 5$ ppm CO, $H_2 + 20$ ppm CO, $H_2 + 25\%$ N_2, $H_2 + 5$ ppm CO $+ 25\%$ N_2 and $H_2 + 20$ ppm CO $+ 25\%$ N_2 contaminated conditions, respectively; row (2): corresponding pattern (i.e., state probability) vectors for each condition.

with a voltage pulse of 5 s duration. Each column depicts a scenario, where the sensor is subjected to different gases at different concentrations. From left to right, the gases are pure H_2, H_2 mixed with 5 ppm CO, 25% N_2 and 25% $N_2 + 5$ ppm CO contaminated conditions, respectively.

For ASSP of the time series data described in section 2.2, maximum entropy partitioning is employed in the radial direction with $|\Sigma_R| = 2$, while using uniform partitioning in the angular direction with $|\Sigma_A| = 3$. Thus, the alphabet size $|\Sigma| \triangleq |\Sigma_R| \times |\Sigma_A| = 6$ and a depth of $D = 1$ have been selected. The pattern vector obtained by constructing the D-Markov machine is a representation of the dynamical system that characterizes the EC sensor operation under a particular operating condition. The state probability vectors are shown as histograms in the bottom row in figure 5. This visualization displays how the structure of the underlying probability distribution changes as the concentration of contaminants or the nature of the poisoning mechanism changes.

To test the robustness of the algorithm, each experiment was performed several times to generate 47 sets of data with different contaminants and the data-set was used to train and test a two-layer feed-forward network, with sigmoid hidden and output neurons. Such networks can classify vectors arbitrarily well, given enough neurons in its hidden layer. The network was trained with scaled conjugate gradient back-propagation [47].

2.5.4. Classification. As an initial benchmark test, 18 of the first 24 pattern vectors were randomly selected and used for training the neural net. The remaining six were used for validation. This was repeated to generate a statistic about the true positive rate and the false positive rate of the classifier.

The results were uniformly consistent and the neural network could correctly classify the four classes of gas mixtures (class 1–4). However, the main focus of this work is to investigate the efficacy of the algorithm in predicting the combination of gaseous contaminants while being trained with only single contaminants. This characterizes a very important scenario in real world CWA monitoring, since even though a classifier may be trained for recognizing single CWA agents, it may be needed to identify that gas in the presence of a myriad of other toxic or non-toxic gases. Even the presence of dust can act as a deterrent to correct classification. For that purpose, in the second phase, the neural net was only trained with patterns corresponding to classes 1, 2, 3 and 4, i.e. pure H_2, $H_2 + 5$ ppm CO, $H_2 + 25\%$ N_2 and $H_2 + 20$ ppm CO, respectively. In the testing phase, however, in addition to all these gases, pattern vectors characterizing two other mixtures of $H_2 + 5$ ppm CO $+ 25\%$ N_2 and $H_2 + 20$ ppm CO $+ 25\%$ N_2 were also fed as input to the trained neural net. The outputs of the net is displayed in table 1.

It may be noted that for data-sets 1 through 24 (corresponding to pure gas or single contaminant conditions), the outputs of the neural net unambiguously predict the class to which they should belong, indicated by $\sim$1 for one and only one class, while being $\sim$0 for all other classes. However, for sets ranging from 25 to 29, the outputs predict membership in both classes 2 and 3, which implies that the pattern contains characteristics derived from both CO and N_2. Only for data-set 28, the classifier puts unequal weight in class 3 compared to class 2. But even that can be easily overcome using thresholds. For example, if the threshold is set as 1%, i.e. a signal is considered to be a member of a particular class if the membership indicator is $\geqslant 0.01$, it can be easily verified that each one of the data-sets 1 through 24 is uniquely and correctly classified. Thus, this method is able to correctly predict contaminant mixtures containing 5 ppm CO and 25% N_2, while having been trained with only the single contaminants separately. However, it cannot be claimed that 1% will serve as the optimum threshold for all contaminant mixtures. A compromise between false positive rate and true positive rate by constructing a receiver-operating characteristic (ROC) curve can be used to find the optimum threshold for a particular target contaminant.

However, the most interesting aspect of this classification scheme manifests itself in the data-sets ranging from 30 to 47. Each and every pattern vector characterizing a mixture of $H_2 + 20$ ppm CO $+ 25\%$ N_2 is wrongly classified as belonging to class 4, rather than a mixture of classes 3 and 4. The reason becomes obvious if the current response and the corresponding state probability vectors shown in columns 3 and 6 in figure 5 are compared. As indicated by column 3 of this figure, $H_2 + 20$ ppm CO poisons the catalyst surface resulting in significantly lowered current compared to pure H_2.

Table 1. Membership indicators for the four classes.

Data set	Pure H_2	H_2 + 5 ppm CO	H_2 + 25% N_2	H_2 + 20 ppm CO	Inference class	Target class
	Class 1	Class 2	Class 3	Class 4		
1	0.9999	0.0001	0.0000	0.0000	1	1
2	0.9998	0.0002	0.0000	0.0000	1	1
3	0.9991	0.0008	0.0000	0.0000	1	1
4	0.9988	0.0008	0.0000	0.0000	1	1
5	0.0000	1.0000	0.0000	0.0000	2	2
6	0.0001	0.9999	0.0000	0.0000	2	2
7	0.0000	1.0000	0.0000	0.0000	2	2
8	0.0000	1.0000	0.0000	0.0000	2	2
9	0.0000	1.0000	0.0000	0.0000	2	2
10	0.0000	1.0000	0.0000	0.0000	2	2
11	0.0000	1.0000	0.0000	0.0000	2	2
12	0.0000	1.0000	0.0000	0.0000	2	2
13	0.0000	1.0000	0.0000	0.0000	2	2
14	0.0000	0.0000	1.0000	0.0000	3	3
15	0.0000	0.0000	1.0000	0.0000	3	3
16	0.0000	0.0000	1.0000	0.0000	3	3
17	0.0000	0.0000	0.0000	1.0000	4	4
18	0.0000	0.0000	0.0000	1.0000	4	4
19	0.0000	0.0000	0.0000	1.0000	4	4
20	0.0000	0.0000	0.0000	1.0000	4	4
21	0.0000	0.0000	0.0000	1.0000	4	4
22	0.0000	0.0000	0.0000	1.0000	4	4
23	0.0000	0.0000	0.0000	1.0000	4	4
24	0.0000	0.0000	0.0000	1.0000	4	4
25	0.0000	0.9876	0.8079	0.0000	2 + 3	2 + 3
26	0.0000	0.4089	0.9451	0.0000	2 + 3	2 + 3
27	0.0000	0.7609	0.8009	0.0000	2 + 3	2 + 3
28	0.0000	0.0479	0.9874	0.0000	2 + 3	2 + 3
29	0.0000	0.6333	0.5095	0.0000	2 + 3	2 + 3
30	0.0000	0.0000	0.0000	1.0000	4	3 + 4
31	0.0000	0.0000	0.0000	1.0000	4	3 + 4
32	0.0000	0.0000	0.0000	1.0000	4	3 + 4
33	0.0000	0.0000	0.0000	1.0000	4	3 + 4
34	0.0000	0.0000	0.0000	1.0000	4	3 + 4
35	0.0000	0.0000	0.0000	1.0000	4	3 + 4
36	0.0000	0.0000	0.0000	1.0000	4	3 + 4
37	0.0000	0.0000	0.0000	1.0000	4	3 + 4
38	0.0000	0.0000	0.0000	1.0000	4	3 + 4
39	0.0000	0.0000	0.0000	1.0000	4	3 + 4
40	0.0000	0.0000	0.0000	1.0000	4	3 + 4
41	0.0000	0.0000	0.0000	1.0000	4	3 + 4
42	0.0000	0.0000	0.0000	1.0000	4	3 + 4
43	0.0000	0.0000	0.0000	1.0000	4	3 + 4
44	0.0000	0.0000	0.0000	1.0000	4	3 + 4
45	0.0000	0.0000	0.0000	1.0000	4	3 + 4
46	0.0000	0.0000	0.0000	1.0000	4	3 + 4
47	0.0000	0.0000	0.0000	1.0000	4	3 + 4

When 25% N_2 is added to make the H_2 + 20 ppm CO + 25% N_2 mixture, the current response very closely resembles the response of the same mixture without the 25% N_2. Therefore, it is clear that the CO surface adsorption on the catalyst surface dominates the performance characteristics, and the addition of the 25% N_2 only slightly dilutes the poisoning level.

This particular situation is a good example that showcases the difficulties associated with the reliable detection of environmental contaminants in practice. The presence of a myriad of possibly harmless gases confuses the detection mechanism leading to unacceptable false alarm rates and missed events. However, the flexibility inherent in the smart EC sensor can be used to mitigate this problem to a large extent. In order to extract more information than available from the data-sets just described, the sensor is next operated at an elevated temperature of 75 °C rather than 65 °C. Since all adsorption processes are exothermic, and the sticking coefficient of the CO on the catalyst surface follows an Arrhenius law, raising the temperature will reduce the surface overage and mitigate the effect of CO on performance. The diffusive processes in the

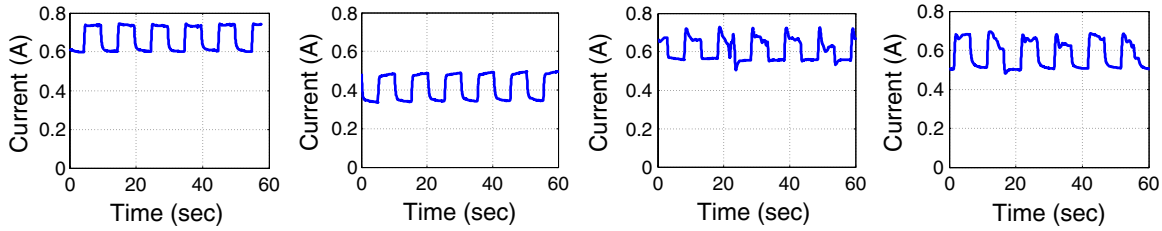

Figure 6. Current response of the EC sensor for (left to right) pure H_2, H_2 + 20 ppm CO, H_2 + 25%N_2 and H_2 + 20 ppm CO + 25% N_2 contaminated conditions, respectively.

Table 2. Membership indicators for the three classes at elevated temperature.

Data set	Pure H_2	H_2 + 25% N_2	H_2 + 20 ppm CO	Inference class	Target class
	Class 1	Class 3	Class 4		
1	0.9932	0.0045	0.0002	1	1
2	0.9983	0.0003	0.0013	1	1
3	0.8493	0.0379	0.0004	1	1
4	0.9977	0.0006	0.0013	1	1
5	0.9931	0.0079	0.0004	1	1
6	0.9715	0.0034	0.0008	1	1
7	0.0009	0.9990	0.0014	3	3
8	0.0005	0.9995	0.0008	3	3
9	0.0009	0.9987	0.0016	3	3
10	0.0006	0.9988	0.0017	3	3
11	0.0003	0.9992	0.0015	3	3
12	0.0006	0.9987	0.0014	3	3
13	0.0007	0.9992	0.0009	3	3
14	0.0008	0.9993	0.0004	3	3
15	0.0014	0.9877	0.0057	3	3
16	0.0003	0.0002	1.0000	4	4
17	0.0004	0.0001	0.9999	4	4
18	0.0003	0.0003	0.9997	4	4
19	0.0003	0.0001	0.9999	4	4
20	0.0008	0.0003	0.9995	4	4
21	0.0005	0.0004	0.9995	4	4
22	0.0001	0.0005	0.9999	4	4
23	0.0003	0.0001	0.9999	4	4
24	0.0004	0.0004	0.9996	4	4
25	0.0001	0.9809	0.7146	3 + 4	3 + 4
26	0.0010	0.9985	0.0476	3 + 4	3 + 4
27	0.0010	0.9974	0.1131	3 + 4	3 + 4
28	0.0003	0.9378	0.2659	3 + 4	3 + 4
29	0.0015	0.9915	0.3288	3 + 4	3 + 4
30	0.0037	0.9978	0.3749	3 + 4	3 + 4
31	0.0004	0.9955	0.2676	3 + 4	3 + 4
32	0.0002	0.9926	0.3158	3 + 4	3 + 4

gas phase being weakly dependent on temperature, the effect due to N_2 will remain relatively unchanged at the elevated temperature.

Following this logic, in the second phase, the same experiments using pure H_2, H_2 + 20 ppm CO, H_2 + 25% N_2 and finally H_2 + 20 ppm CO + 25% N_2 were carried out with the exact same experimental parameters except the temperature was elevated to 75 °C. The pattern vectors produced by analyzing the current response (figure 6) with SDF were passed through the neural network and the output of the net is reported in table 2. The pure gas and the single contaminants are classified successfully, but the major improvement is observed in data-sets 25–32 which correspond to a mixture of H_2 + 20 ppm CO + 25% N_2. Unlike before, the mixture of H_2 + 20 ppm CO + 25% N_2 is correctly classified as belonging to classes 3 and 4.

The inclusion of temperature as an operating parameter thus resulted in much better specificity of the sensor. Utilizing available parameters such as humidity, gas flow rate, etc, and varying them in conjunction with temperature can thus potentially result in a further increase in specificity, more confident detection and lower false alarm rates. Extensively tested and validated, this capability would be a unique asset invaluable in real world toxic vapor identification systems.

3. Summary, conclusions and future work

The work presented in this paper reports the use of a stochastic signal processing tool called SDF for pattern extraction from the EC sensor dynamic response. Perturbing the sensor with an oscillating potential rather than static voltage levels enabled the extraction of statistically rich information from the current response. The shape of the dynamic response is a function of the degree and mechanism of contamination by different species, and therefore carries signatures of the operating condition. The current response to an oscillating perturbation was first transformed into an analytic signal through Hilbert transform and then discritized. A PFSA representation was constructed on the principle of sliding block codes with characteristic state transition matrices. The state probability vectors were then extracted in the form of low-dimensional pattern vectors for the correct classification of gases. Fusing information obtained from operating the sensor at different temperatures, correct classification between single contaminant gases as well as gas mixtures could be achieved with high accuracy and very low false alarm rates.

The optimum parameters for detecting each target contaminant and each target concentration depend on the EC process through which they interact with the electrochemical system. The primary method of CO interaction being surface adsorption on the platinum-based catalyst, in this paper, an elevated temperature operating condition was used in addition to the normal operating temperature to liberate some of the CO from the surface forcing the 20 ppm solution to function effectively with lesser concentration, thus enabling more accurate detection in a mixture of contaminants.

Even though the EC mechanism which governs the interaction of different poisonous gases with the sensor will be widely different from each other, similar considerations

will drive the operating parameter choice in the practical cases of interest. In general, however, if the physicochemical processes involved with the contaminant species involved are considered and proper methodologies are created to separate these effects, the technique described in this paper will be able to obtain improved specificity due to the utilization of dynamic responses over static response. However, extensive testing under strict laboratory conditions will enable this to be claimed with certainty. This will be the natural extension of this research in the future.

In a broader context, the sensors developed here could be networked into large coordinated clusters. The redundancy would greatly increase the veracity of the sensor output, and could also be used to dynamically identify the source location, spread and timing of contamination in urban environments.

References

[1] Janata J and Bezegh A 1988 Chemical sensors *Anal. Chem.* **60** 62R–74R

[2] Janata J 1990 Chemical sensors *Anal. Chem.* **62** 33R–44R

[3] Janata J 1992 Chemical sensors *Anal. Chem.* **64** 196R–219R

[4] Mari C M and Barbi G B 1992 *Electrochemical Gas Sensors* (New York: Springer)

[5] Brett C M A 2001 Electrochemical sensors for environmental monitoring. Strategy and examples *Pure Appl. Chem.* **73** 1969–77

[6] Murthy M, Esayian M, Lee W-K and Zee J W V 2003 The effect of temperature and pressure on the performance of a PEMFC exposed to transient CO concentrations *J. Electrochem. Soc.* **150** A29–34

[7] Zhang J, Thampan T and Datta R 2002 Influence of anode flow rate and cathode oxygen pressure on CO poisoning of proton exchange membrane fuel cells *J. Electrochem. Soc.* **149** A765–72

[8] Hodgson A W E, Jacquinot P and Hauser P C 1999 Electrochemical sensor for the detection of SO_2 in the low-ppb range *Anal. Chem.* **71** 2831–7

[9] Jordan L R and Hauser P C 1997 Electrochemical sensor for acetylene *Anal. Chem.* **69** 2669–72

[10] Blurton K F and Stetter J R 1978 Sensitive electrochemical detector for gas chromatography *J. Chromatogr.* **155** 35–45

[11] Maruyama T, Sasaki S and Saito Y 1987 Potentiometric gas sensor for carbon dioxide using solid electrolytes *Solid State Ion.* **23** 107–12

[12] Yamazoe N and Miura N 1998 Potentiometric gas sensors for oxidic gases *J. Electroceram.* **2** 243–55

[13] Meyerhoff M E 1980 Polymer membrane electrode based potentiometric ammonia gas sensor *Anal. Chem.* **52** 1532–4

[14] Hong H K, Shin H W, Park H S, Yun D H, Kwon C H, Lee K, Kim S T and Moriizumi T 1996 Gas identification using micro gas sensor array and neural-network pattern recognition *Sensors Actuators* B **33** 68–71

[15] Bhambare K S, Gupta S, Mench M M and Ray A 2008 A carbon monoxide sensor in polymer electrolyte fuel cells based on symbolic dynamic filtering *Sensors Actuators* B **134** 803–15

[16] Stetter J R, Jurs P C and Rose S L 1986 Detection of hazardous gases and vapors: pattern recognition analysis of data from an electrochemical sensor array *Anal. Chem.* **58** 860–6

[17] Jazwinski A H 2007 *Stochastic Processes and Filtering Theory* (New York: Dover)

[18] Arulampalam M S, Maskell S, Gordon N and Clapp T 2002 A tutorial on particle filters for online nonlinear/non-Gaussian Bayesian tracking *IEEE Trans. Signal Process.* **50** 174–88

[19] Andrieu C, Doucet A, Singh S and Tadic V B 2004 Particle methods for change detection, system identification, and control *Proc. IEEE* **92** 423–38

[20] Julier S, Uhlmann J and Durrant-Whyte H F 2000 A new method for the nonlinear transformation of means and covariances in filters and estimators *IEEE Trans. Autom. Control* **45** 477–82

[21] Li P and Kadirkamanathan V 2001 Particle filtering based likelihood ratio approach to fault diagnosis in nonlinear stochastic systems *IEEE Trans. Syst. Man Cybern.* C **31** 337–43

[22] Duda R O, Hart P E and Stork D G 2012 *Pattern Classification* (New York: Wiley)

[23] Liu J and Scherpen J 2002 Fault detection method for nonlinear systems based on probabilistic neural network filtering *Int. J. Syst. Sci.* **33** 1039–50

[24] Haykin S 1994 *Neural Networks: A Comprehensive Foundation* (Englewood Cliffs, NJ: Prentice-Hall)

[25] Fukunaga K 1990 *Introduction to Statistical Pattern Recognition* (Amsterdam: Elsevier)

[26] Shawe-Taylor J and Cristianini N 2004 *Kernel Methods for Pattern Analysis* (Cambridge: Cambridge University Press)

[27] Rao C, Ray A, Sarkar S and Yasar M 2009 Review and comparative evaluation of symbolic dynamic filtering for detection of anomaly patterns *Signal Image Video Process.* **3** 101–14

[28] Ray A 2004 Symbolic dynamic analysis of complex systems for anomaly detection *Signal Process.* **84** 1115–30

[29] Lind D A 1995 *An Introduction to Symbolic Dynamics and Coding* (Cambridge: Cambridge University Press)

[30] Duda R, Hart P and Stork D 2001 *Pattern Classification* (New York: Wiley)

[31] Cover T M and Thomas J A 1991 *Elements of Information Theory* (New York: Wiley)

[32] Hopcroft H E, Motwani R and Ullman J D 2001 *Introduction to Automata Theory, Languages, and Computation* 2nd edn (Boston, MA: Addison-Wesley)

[33] Badii R and Politi A 1997 *Complexity Hierarchical Structures and Scaling in Physics* (Cambridge: Cambridge University Press)

[34] Chakraborty S, Sarkar S, Gupta S and Ray A 2008 Damage monitoring of refractory wall in a generic entrained-bed slagging gasification system *Proc. Instn Mech. Eng.* A **222** 791–807

[35] Daw C S, Finney C E A and Tracy E R 2003 A review of symbolic analysis of experimental data *Rev. Sci. Instrum.* **74** 915

[36] Chakraborty S, Ray A, Subbu A and Keller E 2010 Analytic signal space partitioning and symbolic dynamic filtering for degradation monitoring of electric motors *Signal Image Video Process.* **4** 399–403

[37] Chakraborty S, Keller E, Talley J, Srivastav A, Ray A and Kim S 2009 Void fraction measurement in two-phase flow processes via symbolic dynamic filtering of ultrasonic signals *Meas. Sci. Technol.* **20** 023001

[38] Cohen L 1995 *Time–Frequency Analysis* (Upper Saddle River, NJ: Prentice-Hall)

[39] Rajagopalan V and Ray A 2006 Symbolic time series analysis via wavelet-based partitioning *Signal Process.* **86** 3309–20

[40] Mccallum A and Freitag D 2000 *Maximum Entropy Markov Models for Information Extraction and Segmentation* (San Mateo, CA: Morgan Kaufmann) pp 591–8

[41] Friedman N, Geiger D and Goldszmidt M 1997 Bayesian network classifiers *Mach. Learn.* **29** 131–63

[42] Yuan Y and Shaw M J 1995 Induction of fuzzy decision trees *Fuzzy Sets Syst.* **69** 125–39
[43] Cortes C and Vapnik V 1995 Support-vector networks *Mach. Learn.* **20** 273–97
[44] Epanechnikov V A 1969 Non-parametric estimation of a multivariate probability density *Theory Probab. Appl.* **14** 153–8
[45] Beyer K, Goldstein J, Ramakrishnan R and Shaft U 1999 When is nearest neighbor meaningful? *Database Theory—ICDT 99* (*Lecture Notes in Computer Science* vol 1540) ed C Beeri and P Buneman (Berlin: Springer) pp 217–35
[46] Vogel W, Lundquist L, Ross P and Stonehart P 1975 Reaction pathways and poisons: II. The rate controlling step for electrochemical oxidation of hydrogen on Pt in acid and poisoning of the reaction by CO *Electrochim. Acta* **20** 79–93
[47] Møller M F 1993 A scaled conjugate gradient algorithm for fast supervised learning *Neural Netw.* **6** 525–33